Chemical Geology 575 (2021) 120259

Contents lists available at ScienceDirect

Chemical Geology

journal homepage: www.elsevier.com/locate/chemgeo

Molybdenum isotopic evidence for anoxic marine conditions during the end-Permian mass extinction

Yuxu Zhang [a], Hanjie Wen [a,b,*], Chuanwei Zhu [a], Haifeng Fan [a], Jiafei Xiao [a], Jing Wen [a,b]

[a] State Key Laboratory of Ore Deposit Geochemistry, Institute of Geochemistry, Chinese Academy of Sciences, Guiyang 550081, China
[b] College of Earth and Planetary Sciences, University of Chinese Academy of Sciences, Beijing 100049, China

ARTICLE INFO

Editor: Michael E. Boettcher

Keywords:
Mo isotope
Redox condition
End-Permian mass extinction
Meishan section
Dajiang section

ABSTRACT

The end-Permian mass extinction was the most severe biotic crisis of the Phanerozoic. Oceanic anoxia has long been considered one of the main drivers of the biotic crisis. We examined the molybdenum isotope compositions of bulk carbonate samples from two Permian–Triassic boundary sections in southern China: the Meishan Global Stratotype Section and Point and the Dajiang section (an isolated carbonate platform). We also measured the Mo contents of the carbonate phases, oxides, and sulfides of the carbonate samples via sequential extraction to investigate the samples' Mo-bearing minerals. In the Meishan section, from Bed 23 to the middle of Bed 24, the $\delta^{98/95}Mo_{corr.Al}$ values decrease slowly from +0.89‰ to +0.35‰, while from the middle of Bed 24 to Bed 25, the $\delta^{98/95}Mo_{corr.Al}$ values abruptly increase from +0.35‰ to +1.78‰. In the Dajiang section, samples below the mass extinction boundary have relatively low $\delta^{98/95}Mo_{corr.Al}$ values with a narrow variation range (−0.05‰ to +0.46‰; average + 0.19‰); the $\delta^{98/95}Mo_{corr.Al}$ values of the five samples directly above the extinction boundary increase abruptly (vary from +1.38‰ to +1.63‰; average of +1.53‰), and the $\delta^{98/95}Mo_{corr.Al}$ values of other samples above the mass extinction boundary fluctuate slightly before returning to pre-extinction values. The results of the sequential extraction procedure indicate that carbonate-phase Mo accounts for a small portion of the total Mo (average of 13.6 and 18.4 wt% for the Meishan and Dajiang sections, respectively), oxidized and sulfided Mo are the dominant forms in the carbonate samples. Moreover, the carbonate samples with high $\delta^{98/95}$Mo values tend to have high contents of sulfided Mo. We suggest that marine carbonate sediments record paleo-ocean Mo isotopic signals by a mechanism similar to that of other open-ocean sediments (e.g., shales): higher $\delta^{98/95}$Mo values in the sediments indicate a more reducing sedimentary environment. Based on this assumption, the $\delta^{98/95}$Mo values of the studied sections indicate that during the Permian–Triassic transition, oceanic anoxia coincided with or slightly predated the mass extinction, and the ocean anoxic event lasted for a relatively short time, likely less than 0.061 Myr.

1. Introduction

The end-Permian mass extinction was the most severe biotic crisis of the Phanerozoic. Over 90% of marine species became extinct, resulting in the destruction of marine ecosystems (Erwin, 1994; Jin et al., 2000). However, the cause of this mass extinction event is still subject to debate (Chen et al., 2015). A leading hypothesis is that the global oceans, from deep water through the photic zone, became depleted in oxygen (i.e., global anoxia) (e.g., Wignall and Twitchett, 1996; Isozaki, 1997; Grice et al., 2005; Shen et al., 2011). A range of geochemical and paleoecological proxies have been used to constrain the timing of the end-Permian mass extinction and to clarify the marine redox conditions during the Permian–Triassic transition, including authigenic uranium concentrations (Wignall and Twitchett, 1996, 2002), cerium anomaly changes (Kakuwa and Matsumoto, 2006; Algeo et al., 2007), the occurrence of biomarkers indicating photic zone euxinia (Grice et al., 2005), the size distribution of pyrite framboids (e.g., Wignall and Newton, 1998; Wignall et al., 2005; Shen et al., 2007; Bond and Wignall, 2010; Algeo et al., 2011; Chen et al., 2015; Li et al., 2015a), and U isotope compositions ($\delta^{238}U$) and Th/U ratios (Brennecka et al., 2011; Lau et al., 2016; Zhang et al., 2020). However, the details of the timing, extent, and intensity of the anoxia remain controversial.

* Corresponding author at: State Key Laboratory of Ore Deposit Geochemistry (SKLODG), Institute of Geochemistry, Chinese Academy of Sciences, 99 West Lincheng Road, Guiyang, Guizhou Province 550081, China.
E-mail address: wenhanjie@vip.gyig.ac.cn (H. Wen).

https://doi.org/10.1016/j.chemgeo.2021.120259
Received 18 November 2020; Received in revised form 26 March 2021; Accepted 17 April 2021
Available online 21 April 2021

Molybdenum is a redox-sensitive trace metal with a residence time in seawater of about 800 kyr, which greatly exceeds ocean mixing timescales (~1500 yr) (e.g., Emerson and Huested, 1991). Under oxic conditions, light Mo isotopes are preferentially adsorbed by Fe-Mn oxides, resulting in the $\delta^{98/95}$Mo values of oxic sediments varying from −1.0‰ to −0.5‰ (−0.7 ± 0.1‰ on average) (Barling et al., 2001; Siebert et al., 2003; Poulson et al., 2006). Under anoxic conditions, the H_2S concentration is a "geochemical switch" and an important control on Mo isotopic fractionation. When the H_2S concentration of the water column is >100 μmol/L, almost all of the aqueous MoO_4^{2-} species become MoS_4^{2-} species and are precipitated; this process imparts negligible Mo isotope fractionation. Thus, the $\delta^{98/95}$Mo value of euxinic sediment (H_2S > 100 μmol/L) reflects the Mo isotope composition of its overlying seawater (Barling et al., 2001; Arnold et al., 2004; Poulson et al., 2006; Siebert et al., 2006). In contrast, when H_2S concentrations are between 0.1 and 100 μmol/L, MoO_4^{2-}, $MoO_{4-x}S_x^{2-}$, and MoS_4^{2-} coexist in the water column, and only a fraction of the dissolved Mo precipitates and is deposited in the underlying sediments. Therefore, the Mo isotope composition of the sediments varies, with the $\delta^{98/95}$Mo value being between −0.5‰ and + 1.3‰ under dysoxic conditions, and ~ 1.6‰ under anoxic conditions (Anbar, 2004; Tossell, 2005; Poulson et al., 2006; Siebert et al., 2006).

In recent decades, Mo and its isotopes have been used to investigate the paleo-redox conditions of the Earth's atmosphere and oceans (e.g., Barling et al., 2001; Siebert et al., 2003, 2006; Arnold et al., 2004; Wille et al., 2007; Scheiderich et al., 2010; Kendall et al., 2011; Wen et al., 2011, 2015; Zhou et al., 2011, 2012; Scott and Lyons, 2012; Proemse et al., 2013; Kurzweil et al., 2016; Ruebsam et al., 2017; Cheng et al., 2018; Magnall et al., 2018; Chen et al., 2019). These studies have mostly focused on sediments deposited under euxinic conditions (e.g., black shales); however, the sedimentary strata that have recorded important geological events throughout geologic history (especially after the Cambrian) are mostly carbonates. Voegelin et al. (2009) hypothesized negligible Mo isotopic fractionation during Mo uptake into non-euxinic, non-skeletal marine carbonates. The mechanism of this hypothesis is still not well constrained, but it provides an important proxy for tracing oceanic paleo-redox evolution through geologic history. However, one recent study reported a ~ 0.7‰ offset in the $\delta^{98/95}$Mo value between seawater and carbonate-rich sediments (Bura-Nakić et al., 2020). Therefore, it is necessary to understand how Mo isotopes in seawater are preserved in carbonates before using their Mo isotope compositions to reconstruct the Mo isotope evolution of ancient seawater.

In this study, we leached three Mo-associated phases (carbonate, oxide, and sulfide) and measured the Mo isotope compositions of bulk carbonates from two sections in South China (the Meishan and Dajiang sections) to constrain the changes in ocean redox conditions during the mass extinction event at the Permian–Triassic boundary (PTB). Based on these results, we suggest that the intensification of oceanic anoxia coincided with or slightly predated the end-Permian mass extinction, and the ocean anoxia may have lasted for a short period.

2. Geologic setting

During the late Carboniferous to early Permian, Laurentia and Gondwanaland were amalgamated to form Pangea. The Paleo-Tethys Ocean was a horn-shaped open ocean near the middle of the eastern margin of Pangea, and the South China Plate occurred as an isolated island in the Paleo-Tethys Ocean (Fig. 1a) (Nie, 1991; Yin and Song, 2013). At the PTB, the centre of the South China Plate was marked by the Yangtze carbonate platform, of which the northern and southern margins were deep-water basin facies (Fig. 1b) (Yin et al., 2014). These basins had different origins on the northern and southern margins. The northern basin has a normal sedimentary framework indicative of a marginal sea with continental shelf–continental slope–deep sea facies. In contrast, the southern basin was a NE–SW-trending rift zone controlled by stretching, along which isolated carbonate platforms developed within and between the rift zone and the Yangtze Platform (Lehrmann et al., 1998, 2003; Yin et al., 2014). Thus, the South China Plate is an ideal area for studying PTB marine and terrigenous strata and related geological events. We chose the Meishan and Dajiang sections as being representative of the northern and southern marginal basins of the Yangtze Platform, respectively.

2.1. Meishan section

The Meishan section is located in Meishan Town, Changxing County, Zhejiang Province, China. The section is ideal for investigating the evolution of the biota and environment during the Permian–Triassic transition due to the excellent preservation of fossils. The section was established as the Global Stratotype Section and Point of the PTB in 2001 (Yin et al., 2001). During the Permian–Triassic transition, the Meishan section was located on the northern margin of the Yangtze platform, which was a relatively deep-water platform–margin slope and an intermediate or transitional zone between the shallow shelf and the deep-water basin (Fig. 1b); the section's water depth was ~150 m (He et al., 2005; Li et al., 2015a). The stratigraphic sequence of the Meishan section, from bottom to top, consists of bioclastic limestone of the late Permian Changhsing Formation and mudstone and muddy limestone of the early Triassic Yinkeng Formation (Fig. 1c). The main mass extinction boundary of the end-Permian mass extinction is thought to be at the bottom of Bed 25 (Yang et al., 1993; Yin, 1996; Xie et al., 2005; Yin et al., 2007; Song et al., 2013). The bottom of Bed 27c has been identified as the PTB where the conodont *H.parvus* was first discovered (Yin et al., 2001).

2.2. Dajiang section

The Dajiang section is located in Bianyang Town, Luodian County, Guizhou Province, China. Due to the continuous record and good exposure of the PTB strata, the Dajiang section is ideal for investigating shallow water platform facies. As a result of the eruption of the Emeishan basalt and the formation of related basement fractures during the late Permian, the northern margin of the Yangtze Platform exhibits an apparent paleogeographic pattern of platform–platform margin–basin, with some isolated carbonate platforms within the platform margin and basin zones. The Nanpanjing Basin was located on the southern margin of the Yangtze Platform, and the isolated carbonate platform, which was located on the southern margin of the Nanpanjing Basin, is called the Great Bank of Guizhou (Lehrmann et al., 1998, 2005). The Dajiang section was located on the interior of the Great Bank of Guizhou (Fig. 1b), and the water depth was <20–30 m (Lehrmann et al., 1998).

The stratigraphic sequence of the Dajiang section, from bottom to top, consists of bioclastic limestone of the Upper Permian Wujiaping Formation and massive microbialite and thin- to medium-bedded limestone of the Lower Triassic Daye Formation (Fig. 1d). In this section, the mass extinction boundary of the end-Permian mass extinction is thought to lie in the interface between the bioclastic limestone and the microbialite. However, the precise location of the PTB is controversial. Some researchers have proposed that the boundary is located within the microbialite (Lehrmann et al., 2003; Chen et al., 2009), while others suggest that the PTB coincides with the mass extinction boundary between the bioclastic limestone and the microbialite (Ezaki et al., 2003; Jiang et al., 2014; Song et al., 2014).

3. Samples and methods

3.1. Sampling and sample preparation

Samples were obtained from the two PTB sections, including 24 carbonate and 4 claystone samples from the Meishan section and 24 carbonate samples from the Dajiang section. All samples were freshly

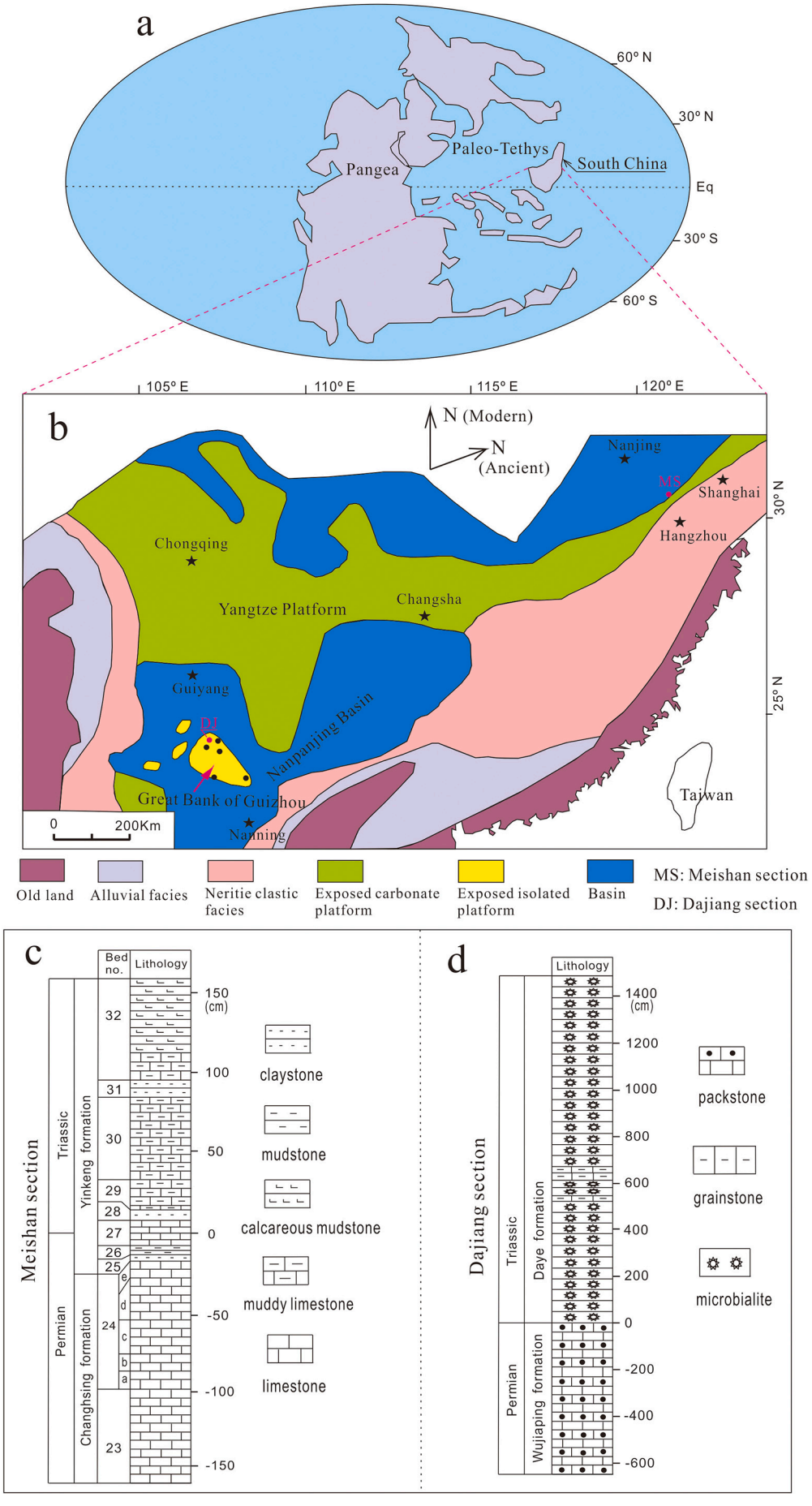

(caption on next page)

Fig. 1. (a) Paleogeography of the Paleo-Tethys Ocean and location of the South China Plate during the Permian–Triassic transition (modified from Ziegler, 1988); (b) simplified paleogeographic map of southern China during the Permian–Triassic transition (modified from Yin et al., 2014); (c) lithostratigraphic profile of the Meishan section; and (d) lithostratigraphic profile of the Dajiang section.

exposed. Prior to geochemical analysis, each sample was cleaned with deionized water and dried, and then crushed to 200 mesh (0.074 mm). All the acids used in this study were purified by sub-boiling distillation; the water used was 18.2 MΩ grade obtained from a Millipore system.

3.2. Major and trace element analysis

The major and trace elements were analysed using X-ray fluorescence (Axios, PW4400) and inductively coupled plasma–mass spectrometry (PE ELAN DRC-e), respectively, at the State Key Laboratory of Ore Deposit Geochemistry, Institute of Geochemistry, Chinese Academy of Sciences. The analytical uncertainty of the elemental contents was generally better than 5%.

3.3. Analysis of Mo phases

Our sequential extraction method used HAc, HCl, and HNO_3 as the extracting solutions to draw the carbonate-phase, oxidized, and sulfided Mo from the samples, respectively (Nothdurft et al., 2004; Rock and Mineral Analysis Group, 2011; Rongemaille et al., 2011; Cao et al., 2020). First, a 0.2 g subsample of each powdered sample was weighed and placed in a 50 mL centrifuge tube with 30 mL of 1.5 mol/L HAc. After the strong reaction of the carbonate with the HAc subsided and stabilized, the centrifuge tubes were closed and shaken using an oscillator for at least 24 h. Subsequently, each mixture was centrifuged to separate the supernatant from the residue. The supernatants were evaporated to dryness, dissolved in 0.15 mol/L HNO_3, and analysed to determine their HAc-phase Mo (carbonate-phase Mo) concentrations (Nothdurft et al., 2004; Rongemaille et al., 2011; Cao et al., 2020). Then, 20 mL of 3 mol/L HCl was added to digest the residues, and the centrifuge tubes were heated in a boiling water bath for 1 h. The solution aliquots were centrifuged after cooling. The supernatants were transferred to PTFE beakers that were heated on a hot plate at 120 °C to evaporate the liquid. After the supernatants had dried, they were dissolved in 0.15 mol/L HNO_3 and analysed to determine their HCl-phase Mo (oxidized Mo) concentrations. Next, 10 mL of HNO_3 was added to the centrifuge tubes to dissolve the residues, the solutions were transferred to PTFE beakers, and the beakers were heated on a hot plate at 120 °C for 8 h. Quantitative filter paper was used to filter the solution aliquots after cooling. The filtrates were evaporated to dryness, dissolved in 0.15 mol/L HNO_3, and analysed to determine their HNO_3-phase Mo (sulfided Mo) concentrations (Rock and Mineral Analysis Group, 2011). The residues were transferred from the filter paper to crucibles for ashing. Aqua regia and HF were added to digest the samples. Finally, the samples were dissolved in 0.15 mol/L HNO_3 and analysed to determine their residue-phase Mo concentrations. The HAc-phase, HCl-phase, HNO_3-phase, and residue-phase Mo concentrations were added to obtain the total Mo concentrations of the samples.

3.4. Mo isotope analysis of bulk samples

Sample purification, Mo isotope measurements, and data processing are described in detail by Zhang et al. (2009), Wen et al. (2010, 2011, 2015), and Liu et al. (2016). Briefly, after determining the samples' Mo contents, a powdered subsample containing >0.15 μg of Mo was digested with 6 mol/L HCl and a trace amount of 30% H_2O_2 to remove the carbonate matrix. Once the strong reaction between the carbonate and the HCl subsided and stabilized, the beakers were capped and placed on a hot plate at 120 °C for at least 24 h. Subsequently, the residual material in the beakers was separated from the solution by centrifugation, and the solution was transferred into another PTFE beaker. Then, 4 mL of 48% (*v*/v) HF and 8 mL of 15 mol/L HNO_3 were added to dissolve the residual material, and the beakers were heated on a hot plate at 120 °C. After complete dissolution, the samples were evaporated to dryness. Then, 10 mL of 7.5 mol/L HNO_3 was added to the beaker and mixed with the supernatant. A ^{97}Mo-^{100}Mo double-spike solution (^{97}Mo/^{100}Mo ≈ 1; see Liu et al. (2016) for more information about the double-spike solution) was added to each sample to achieve a ratio of Mo spike to sample of ~2. The samples were then placed in an oscillator for 24 h to allow them to fully react and attain isotopic equilibrium. Samples were then evaporated to dryness on a hot plate at 100 °C, and 6–10 mL of 6 mol/L HCl was added to dissolve the residues. An improved anion–cation exchange resin double-column procedure was used to separate the Mo from other elements, as described in Table 1 (Zhang et al., 2009; Wen et al., 2015; Liu et al., 2016). This method yields Mo recovery of 97.49 ± 0.27%; and the elements that potentially interfere with the Mo isotopes, including Zr, Ru, Fe, Mn, and other interfering matrix elements, were present in negligible amounts relative to the amount of Mo (Zhang et al., 2009).

The Mo isotope ratio measurements were performed on a Neptune Plus multicollector inductively coupled plasma mass spectrometer (MC-ICP-MS) (Thermo Fisher Scientific, Germany) at the State Key Laboratory of Ore Deposit Geochemistry, Institute of Geochemistry, Chinese Academy of Sciences. The purified Mo from the samples was dissolved in 0.15 mol/L HNO_3 for analysis by MC–IC–MS in low resolution with a Pt 'Jet' sampler and Ni 'x-type' skimmer cones. A Teflon nebulizer with an uptake rate of 50 μL/min was used for sample introduction. The analysed sample solutions had Mo concentrations of ~0.15 μg/mL. Signal acquisition was performed using the following collector configurations: $^{91}Zr^+$, $^{94}Mo^+$, $^{95}Mo^+$, $^{96}Mo^+$, $^{97}Mo^+$, $^{98}Mo^+$, $^{99}Ru^+$, and $^{100}Mo^+$ ion beams were collected by Faraday cups at the L4, L2, L1, C, H1, H2, H3, and H4 positions, respectively. These parameters resulted in a total Mo signal intensity of 120–150 V ppm^{-1}. All the samples and reference solutions were run in 3 blocks of 15 cycles of measurements for each **amu**. After each run, the sample-introduction system was rinsed with 0.6 mol/L HNO_3 until the signal intensity reached the original background level (~2 mV of ^{96}Mo, which generally took about 3 min).

Double-spike data reduction was performed offline using a MATLAB-based script, which is described in detail by Siebert et al. (2001) and Li et al. (2011, 2015b). Nägler et al. (2014) suggested setting the $\delta^{98/95}$Mo of NIST SRM 3134 to +0.25‰, which allows the canonical values of +2.3‰ for seawater and − 0.7‰ for marine Fe-Mn precipitates to be used for discussion and facilitates the comparison of existing and new data (Greber et al., 2012; Goldberg et al., 2013; Wen et al., 2015; Liu et al., 2016). Therefore, the final $\delta^{98/95}$Mo values relative to NIST SRM 3134 = 0.25‰ were defined by the following relationship:

$$\delta^{98/95}\,\mathrm{Mo}(‰) = \left\{ \left(^{98}\mathrm{Mo}/^{95}\mathrm{Mo}\right)_{\mathrm{sample}} \Big/ \left[\left(^{98}\mathrm{Mo}/^{95}\mathrm{Mo}\right)_{\mathrm{NIST\ 3134}} \times 0.99975 \right] - 1 \right\} \times 1000$$

Table 1
Molybdenum chemical purification procedure.

Process	Reagent	Volume/mL
Column #1: 5 mL Dowex AG 1 − X8 (100–200 mesh)		
Clean	1 mol/L HCl	40
Condition	6 mol/L HCl	20
Load sample	Sample solution	3–8
Wash	6 mol/L HCl	40
Collect Mo	1 mol/L HCl	45
Collect Mo	5 mol/L HNO_3	30
Column #2: 5 mL Dowex AG 50 W − X8 (200–400 mesh)		
Condition	1.4 mol/L HCl	30
Load sample	Sample solution	≤3
Collect Mo	1.4 mol/L HCl	11

The $\delta^{98/95}$Mo values of the four Mo reference standards used in this study, which were prepared to monitor the chemical separation and mass spectrometry measurements, are listed in Table 2.

4. Results

4.1. Three-phase Mo extraction results

The carbonate-, oxide-, and sulfide-associated Mo contents of the carbonate samples from the two sections are listed in Table 3 and shown in Figs. 2 and 3. In samples from both sections, the carbonate-phase Mo is a relatively minor proportion of the total Mo.

4.1.1. Meishan section

For the Meishan section, the sulfided Mo of the carbonate samples ranges from 42.3 to 80.8 wt% (55.7 wt% on average), the oxidized Mo ranges from 7.75 to 40.6 wt% (25.7 wt% on average), and the carbonate-phase Mo ranges from 3.52 to 21.0 wt% (13.6 wt% on average). For the three carbonate samples from the Meishan section with high $\delta^{98/95}$Mo values (+1.03‰ to +1.41‰; samples B-24-9, B-27-1, and B-27-2; see Table 4), the carbonate-phase Mo ranges from 3.52 to 10.2 wt% (6.03 wt % on average), the oxidized Mo ranges from 7.75 to 13.9 wt% (11.3 wt% on average), and the sulfided Mo ranges from 67.5 to 80.8 wt% (75.2 wt % on average).

4.1.2. Dajiang section

For the Dajiang section, the sulfided Mo of the carbonate samples ranges from 24.9 to 71.7 wt% (45.3 wt% on average), the oxidized Mo from 8.50 to 56.8 wt% (34.6 wt% on average), and the carbonate-phase Mo from 12.2 to 23.8 wt% (18.4 wt% on average). The five Dajiang section carbonate samples with high $\delta^{98/95}$Mo values (+1.32‰ to +1.56‰; samples TDJ-1-1, TDJ-1-2, TDJ-1-3, TDJ-2, and TDJ-3; see Table 5) contain carbonate-phase Mo of 12.2–19.2 wt% (16.1 wt% on average), oxidized Mo of 8.50–16.2 wt% (14.4 wt% on average), and sulfided Mo of 64.2–71.7 wt% (68.4 wt% on average).

Table 2
The $\delta^{98/95}$Mo values of Mo reference materials.

Mo Reference Material	$\delta^{98/95}$Mo (‰) (2sd, $n = 6$) This Study	$\delta^{98/95}$Mo (‰) (2sd) Previous Studies	
NOD-P-1	−0.65 ± 0.08	−0.63*	Barling et al. (2001)
		−0.66 ± 0.05	Li et al. (2015b)
SCo-1	−0.25 ± 0.09	−0.24 ± 0.06	Li et al. (2015b)
SC + 1 of Sigma-Aldrich Mo	+1.79 ± 0.10	+1.67 ± 0.41	Wen et al. (2010)
		+1.84 ± 0.09	Liu et al. (2016)
SC-1 of Sigma-Aldrich Mo	−1.40 ± 0.07	−1.38 ± 0.29	Wen et al. (2010)
		−1.42 ± 0.06	Liu et al. (2016)

*$\delta^{98/95}$Mo was calculated from $\delta^{97/95}$Mo.

4.2. Mo isotopes and major elements

4.2.1. Meishan section

The $\delta^{98/95}$Mo values and Mo, Al, $CaCO_3$, and $MgCO_3$ contents and Mn/Sr ratios of the Meishan section samples are reported in Table 4 and Fig. 4.

Carbonate samples: The ranges of Mo, Al, $CaCO_3$, and $MgCO_3$ contents for the 24 carbonate samples are 0.07–7.68 μg/g, 0.22%–6.23%, 18.1%–86.1%, and 0.83%–17.3%, respectively. The Mn/Sr ratios of the carbonate samples range from 0.05 to 4.13. Some of these samples are from Beds 23–27, which have Mn/Sr ratios of 0.05–1.56. The $\delta^{98/95}$Mo values of all the carbonate samples vary from −0.13‰ to +1.41‰ (Table 4). From Bed 23 to the middle of Bed 24, the $\delta^{98/95}$Mo values decrease slowly from +0.86‰ to +0.34‰. Then, the $\delta^{98/95}$Mo values increase slightly and then abruptly to a maximum of +1.41‰ at the top of Bed 24. Above Bed 27, the $\delta^{98/95}$Mo values decrease to a minimum of −0.13‰ in Bed 29; they remain below +0.56‰ until Bed 32 (Fig. 4a).

Claystone samples: The $\delta^{98/95}$Mo values of the four claystone samples vary from −0.02‰ to +1.38‰. The $\delta^{98/95}$Mo value of claystone sample B-25-1 is +1.38‰, and the $\delta^{98/95}$Mo values of the other samples vary from −0.02‰ to +0.39‰ (+0.22‰ on average, approximating to the upper crustal mean value) (Table 4). The Mo, Al, $CaCO_3$, and $MgCO_3$ contents are 0.55–5.98 μg/g, 8.10%–10.7%, 2.78%–10.3%, and 5.31%–6.49%, respectively. Previous studies suggested these claystones were deposited directly into the ocean as eruptive material during a period of active volcanism (e.g., Yang et al., 1993; Yin, 1996; Cao and Zheng, 2009). We assume that the sample with the minimum Mo contents and $\delta^{98/95}$Mo value of ~0 (B-28-1: Mo content of 0.55 μg/g and $\delta^{98/95}$Mo of −0.02‰) represents the approximate Mo isotope composition of the primary eruptive materials, whereas the sample with the maximum Mo content and maximum $\delta^{98/95}$Mo value (B-25-1: Mo content of 5.98 μg/g, ~11 times that of B-28-1, and $\delta^{98/95}$Mo of +1.38‰) may record the Mo isotope composition of coeval ancient seawater.

4.2.2. Dajiang section

Carbonates: The Mo, Al, $CaCO_3$, and $MgCO_3$ contents of the 24 carbonate samples are 0.12–2.67 μg/g, 0.01%–0.33%, 60.0%–92.3%, and 0.91%–33.6%, respectively, and the total carbonate ($CaCO_3$ + $MgCO_3$) contents are 88.7%–99.5%. The Mn/Sr ratios of the carbonate samples are 0.16–0.92 (Table 5). The $\delta^{98/95}$Mo values of the carbonate samples from the Dajiang section vary from −0.20‰ to +1.56‰ (Table 5) and are shown in Fig. 5a. The $\delta^{98/95}$Mo values of the samples below the mass extinction boundary are lower (average of +0.19‰) relative to the $\delta^{98/95}$Mo values of the five samples just above the boundary (average of +1.44‰); above the boundary the $\delta^{98/95}$Mo values decrease abruptly and return to pre-extinction values, followed by a slight increase (sample TDJ-7, $\delta^{98/95}$Mo = +0.83‰). Finally, the $\delta^{98/95}$Mo values decrease again and remain at pre-extinction levels.

5. Discussion

5.1. Carbonate Mo isotope compositions and implications for the paleo-ocean environment

Voegelin et al. (2010) investigated black shale and carbonate Mo isotope compositions of samples from a late Archean drill core and found that both sample types had consistent $\delta^{98/95}$Mo variation trends. Bura-Nakić et al. (2020) studied the Mo isotope compositions of anoxic carbonate-rich sediments from a semi-enclosed karstic marine lake on the Island of Mljet in the Adriatic Sea and found that samples from a core

Table 3
Carbonate-phase Mo, oxidized Mo, and sulfided Mo contents of each sample obtained from the sequential extraction procedure.

Meishan section				Dajiang section			
Samples	carbonate-phase Mo (%)	oxidized Mo (%)	sulfided Mo (%)	Samples	carbonate-phase Mo (%)	oxidized Mo (%)	sulfided Mo (%)
B-27-2	4.38	7.75	80.8	TDJ-7	18.3	38.1	37.8
B-27-1	3.52	12.2	77.4	TDJ-6	16.5	56.8	25.1
B-24-9	10.2	13.9	67.5	TDJ-4	17.5	50.1	28.2
B-24-8	21.0	18.6	55.8	TDJ-3	12.2	15.5	70.6
B-24-7	15.1	28.2	53.2	TDJ-2	15.4	16.2	67.3
B-24-6	19.9	30.8	45.7	TDJ-1-3	14.7	16.1	68.2
B-24-5	17.6	30.1	48.8	TDJ-1-2	18.8	8.50	71.7
B-24-4	11.8	40.6	42.3	TDJ-1-1	19.2	15.7	64.2
B-24-3	11.2	40.2	44.4	PDJ-0	23.8	42.3	32.9
B-24-2	18.5	29.2	47.7	PDJ-1	20.8	42.2	36.0
B-24-1	16.5	31.0	48.8	PDJ-2	23.0	50.3	25.7
				PDJ-3	17.3	45.5	36.2
				PDJ-4	21.9	52.2	24.9

obtained at 30 m water depth had $\delta^{98/95}$Mo values between +1.38 to +1.78‰ (+1.64‰ on average; $n = 16$; samples from 5 to 39 cm below the sediment surface). In that study, only the uppermost sample (from 1 cm depth) had a lower δ^{98}Mo value (+1.02‰); these results were consistent with the variation of Mo isotope compositions from open-ocean anoxic sediments (Poulson et al., 2006). However, the mechanism controlling the Mo isotope compositions is still unclear.

In the modern ocean, under oxic conditions, lighter Mo isotopes tend to be absorbed by Fe-Mn oxides, which results in the enrichment of heavier Mo isotopes in seawater. In contrast, under anoxic to euxinic conditions, seawater Mo precipitates rapidly into the sediments in the form of Mo sulfide under high H_2S concentrations; during this precipitation reaction, Mo isotopes are weakly fractionated (e.g., Barling et al., 2001; Siebert et al., 2003; Barling and Anbar, 2004; Poulson-Brucker and McManus, 2009). These processes are the basis for using Mo isotope compositions to trace oceanic paleo-redox conditions (e.g., Siebert et al., 2003; Arnold et al., 2004; Kendall et al., 2009; Voegelin et al., 2009; Duan et al., 2010). Under oxic conditions, the Mo absorbed by the Fe-Mn oxides is preserved in the form of the oxides in the sediments (presumably MoO_3; Tossell, 2005; Poulson et al., 2006; Algeo and Tribovillard, 2009; Goldberg et al., 2009), whereas under reducing conditions, Mo is preserved in the form of the sulfides in sediments (e.g., Helz et al., 1996; Erickson and Helz, 2000; Tossell, 2005; Poulson et al., 2006). Therefore, determining the contents of the carbonate, oxidized, and sulfide phases of the Mo in the sediments is essential when studying the Mo isotope compositions of marine carbonates.

The relative proportions of different Mo forms in carbonates are likely to change during late diagenesis. Huang et al. (2008) studied the Sr isotope composition of marine carbonates collected from the Zhongliang Mountain PTB sections (Chongqing, Southwestern China) and determined that carbonates with low Mn/Sr ratios (<2) were not significantly altered by diagenesis and have retained the geochemical signature from the original seawater. All of the carbonate samples from the Dajiang section and the carbonate samples from Beds 23–27 in the Meishan section have Mn/Sr ratios of <2 (Tables 4 and 5); thus, late diagenesis had a limited influence on the Mo isotopic information of these samples.

The two sections examined here yielded samples with relatively higher $\delta^{98/95}$Mo values (+1.03‰ to +1.56‰) and relatively lower $\delta^{98/95}$Mo values (−0.08‰ to +0.88‰); the carbonate-phase Mo contents are low (average of 13.6% for the Meishan section and 18.4% for the Dajiang section), indicating that the oxidized and sulfided Mo contents are the dominant forms of Mo in the samples (Table 3; Fig. 2). Moreover, the oxidized Mo contents are negatively correlated with $\delta^{98/95}$Mo values, and sulfided Mo contents are positively correlated with $\delta^{98/95}$Mo values (Fig. 3). The ratio between the oxidized and sulfided Mo contents in the carbonate samples may reflect the redox state of the seawater to some extent. When seawater gradually becomes anoxic, the contents of oxidized Mo in carbonate sediments gradually decrease while the contents of sulfided Mo gradually increase, leading to a gradual increase in the $\delta^{98/95}$Mo values of the carbonate sediments. We suggest that the Mo isotope data of the carbonates of this study reflect the three depositional forms of Mo; i.e., the Mo preserved in the carbonate sediments in the form of pore water or inclusions, the oxidized Mo absorbed by Fe-Mn oxides, and the sulfided Mo. The Mo isotopic signature is indicative of the dominant accumulation mechanism of authigenic Mo. Thus, the mechanism by which Mo isotopes are recorded in marine carbonate sediments may be similar to that in other open-ocean sediments, such as shales.

5.2. $\delta^{98/95}$Mo and oceanic paleo-redox conditions

5.2.1. Variations in $\delta^{98/95}$Mo and implications

The application of the Mo isotopic system to the reconstruction of oceanic paleo-redox conditions relies on mass balance between the oxic and reducing Mo sinks (Arnold et al., 2004; Poulson et al., 2006). Modern marine sediments record two important Mo isotopic fractionations: Fe-Mn oxide absorbing Mo under oxic conditions (about −3‰; Barling et al., 2001; Siebert et al., 2003; Poulson et al., 2006; Wasylenki et al., 2008) and Mo isotopic fractionation caused by the generation of thiomolybdate in seawater under anoxic conditions.

Under anoxic conditions, the H_2S concentration is a geochemical switch and an important control on Mo isotopic fractionation. At H_2S concentrations of >100 μmol/L, Mo isotopic fractionation is negligible, while at H_2S concentrations of <100 μmol/L, Mo isotopes are weakly fractionated (about −0.7‰) (Zheng et al., 2000; Siebert et al., 2003; Arnold et al., 2004; Nägler et al., 2005; Poulson et al., 2006; Neubert et al., 2008; Kendall et al., 2017). Under suboxic conditions, the recorded $\delta^{98/95}$Mo values of marine sediments are between those of Fe-Mn oxides and anoxic sediments (Siebert et al., 2003, 2006; Arnold et al., 2004; Poulson et al., 2006; Neubert et al., 2008; Poulson-Brucker and McManus, 2009). Thus, higher $\delta^{98/95}$Mo values in sediments indicate a more reducing precipitation environment, which is consistent with the pattern of redox–$\delta^{98/95}$Mo covariation in modern marine environments, in which the highest $\delta^{98/95}$Mo values are found in the most euxinic facies (e.g., Poulson et al., 2006; Siebert et al., 2006; Poulson-Brucker and McManus, 2009; Herrmann et al., 2012).

From the late Permian to the early Triassic, the $\delta^{98/95}$Mo values of seawater were + 2.23‰ to +2.40‰ (Zhou et al., 2012; Proemse et al., 2013; Ruebsam et al., 2017; Chen et al., 2019), similar to modern seawater (+2.22‰ to +2.50‰; +2.34‰ on average) (Barling et al., 2001; Siebert et al., 2003; Arnold et al., 2004), suggesting that the Mo isotopic fractionation model for the modern ocean can be used to evaluate Mo isotopic fractionation in the paleo-ocean during the PTB.

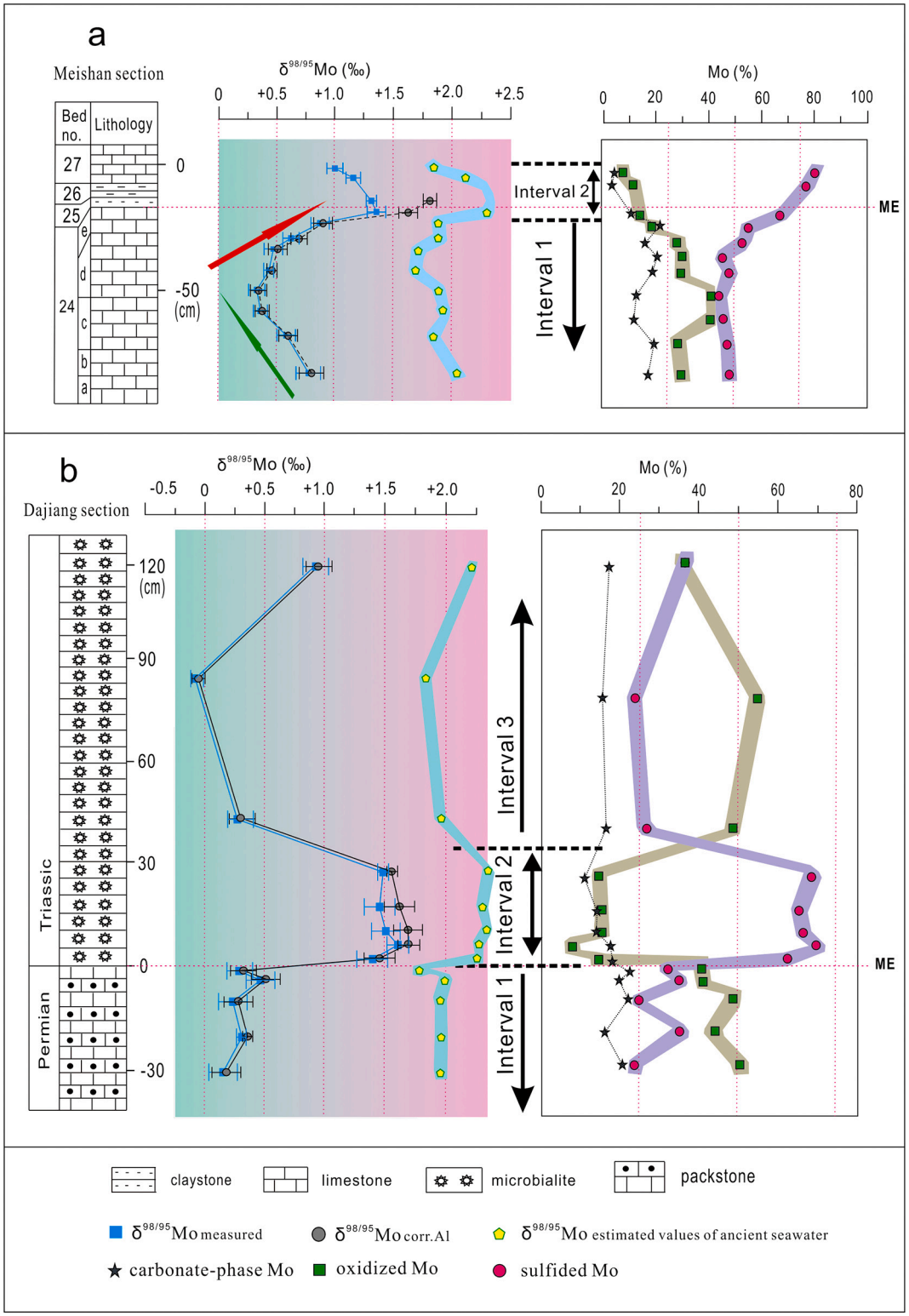

Fig. 2. $\delta^{98/95}$Mo values and the carbonate-phase Mo, oxidized Mo, and sulfided Mo contents of the samples. Estimated $\delta^{98/95}$Mo values of ancient seawater ($\delta^{98/95}Mo_{estimated\ values\ of\ ancient\ seawater}$) and the calculation method are shown in Supplementary Table S1.

5.2.2. $\delta^{98/95}$Mo and oceanic paleo-redox conditions of the Meishan section

The Al/Mo ratios of the samples above the PTB in the Meishan section (samples B-27-3 to B-32-3) are so high (Table 4) that the authigenic Mo contents are extremely low or negative when Al is used to recalculate the $\delta^{98/95}$Mo values using the method of Voegelin et al. (2009). Furthermore, the $\delta^{98/95}$Mo values of these samples vary from −0.13‰ to +0.56‰ (+0.27‰ on average), which is close to the $\delta^{98/95}$Mo of terrigenous detritus (~0.0‰; Siebert et al., 2003; Poulson et al., 2006; Voegelin et al., 2009). Given that we cannot determine whether the Mo in these samples is from terrigenous detritus or ancient seawater, these samples are not considered further in this study. Two samples below the PTB (B-27-2 from Bed 27b and B-27-1 from Bed 27a) have $\delta^{98/95}$Mo

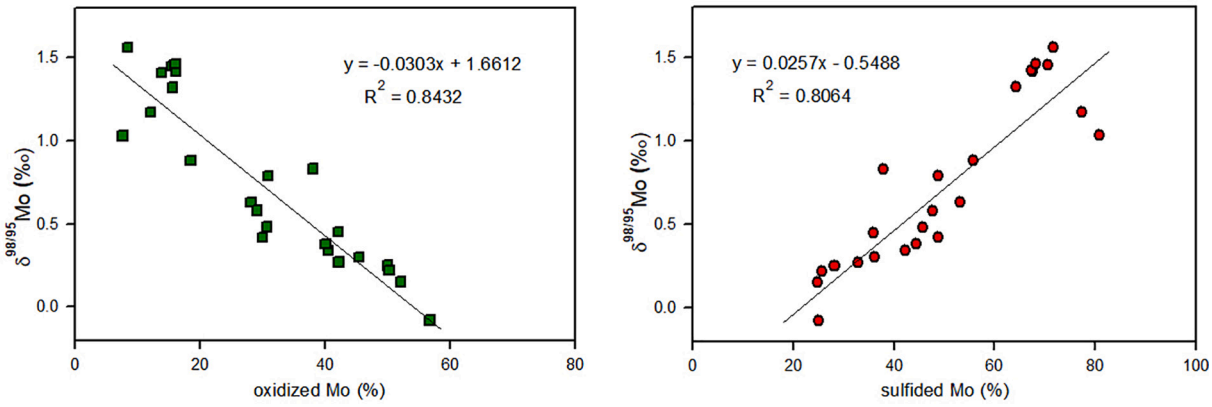

Fig. 3. Relationship between $\delta^{98/95}$Mo values and oxide- and sulfide-associated Mo contents of the carbonate samples.

Table 4
Molybdenum isotope compositions and major elemental contents (Mo, Al, $CaCO_3$, $MgCO_3$, and Mn/Sr) of the Meishan section samples.

Bed no.		Samples	Thickness (cm)	Lithology	$\delta^{98/95}$Mo (‰) (2SD, $N = 3$)	$\delta^{98/95}Mo_{corr.Al}$ (‰)	Mo (μg/g)	Al (%)	$CaCO_3$ (%)	$MgCO_3$ (%)	Ca + Mg (%)	Mn/Sr	Al/Mo ($\times 10^4$)
32		B-32-3	20	calcareous	+0.56 ± 0.14		0.37	6.23	18.1	5.27	23.4	2.76	17
		B-32-2	20	mudstone	+0.39 ± 0.06		0.54	5.90	19.5	10.4	29.9	4.01	11
		B-32-1	20	muddy limestone	+0.37 ± 0.06		0.30	5.22	26.9	12.5	39.4	4.13	17
31		B-31–2	5	claystone	+0.39 ± 0.11		1.90	10.4	3.78	5.38	9.15	0.39	5.5
		B-31–1	4		+0.29 ± 0.04		1.56	10.7	2.78	5.65	8.43	0.97	6.9
30		B-30-3	18	muddy	+0.43 ± 0.05		0.07	3.24	35.8	17.3	53.1	2.70	46
		B-30-2	18	limestone	+0.12 ± 0.04		0.22	4.27	29.8	16.8	46.6	2.98	19
		B-30-1	18		+0.08 ± 0.03		0.21	5.02	21.8	12.8	34.6	3.01	24
29		B-29-1	20	muddy limestone	−0.13 ± 0.09		0.61	6.15	19.1	11.6	30.7	2.98	10
28		B-28-1	6	claystone	−0.02 ± 0.10		0.55	8.10	10.3	6.49	18.8	2.28	15
27	27d	B-27-4	4	limestone	+0.32 ± 0.02		0.35	2.57	49.1	8.19	57.3	1.56	7.3
	27c	B-27-3	4		+0.49 ± 0.05		0.37	2.09	43.8	13.8	57.6	1.46	5.7
	27b	B-27-2	4		+1.03 ± 0.06		0.21	1.96	50.1	12.2	62.3	1.54	9.3
	27a	B-27-1	4		+1.17 ± 0.05		0.21	2.21	53.0	10.1	63.1	1.56	11
25		B-25-1	4	claystone	+1.38 ± 0.04	+1.78	5.98	10.1	4.18	5.31	9.48	0.24	1.7
24	24e	B-24-9	3	limestone	+1.41 ± 0.08	+1.56	2.46	1.70	59.9	1.67	61.6	1.08	0.69
		B-24-8	7		+0.88 ± 0.08	+0.89	2.17	0.24	85.6	1.53	87.1	0.56	0.11
	24d	B-24-7	4	limestone	+0.63 ± 0.07	+0.69	1.08	0.73	61.4	0.83	62.2	0.69	0.68
		B-24-6	6		+0.48 ± 0.08	+0.51	0.88	0.36	78.2	1.28	79.5	0.39	0.41
		B-24-5	10		+0.42 ± 0.02	+0.43	1.11	0.24	82.7	0.97	83.7	0.19	0.22
		B-24-4	6		+0.34 ± 0.07	+0.35	7.68	0.89	62.0	1.01	63.0	0.36	0.12
	24c	B-24-3	10	limestone	+0.38 ± 0.06	+0.39	2.99	0.58	71.1	0.97	72.1	0.24	0.19
		B-24-2	11		+0.58 ± 0.08	+0.59	2.38	0.40	77.2	1.53	78.7	0.12	0.17
	24b,24a	B-24-1	23	limestone	+0.79 ± 0.11	+0.81	1.47	0.28	80.3	1.32	81.6	0.09	0.19
23		B-23-10	4	limestone	+0.77 ± 0.03	+0.79	3.95	0.60	58.8	1.04	59.8	0.16	0.15
		B-23-9	7		+0.77 ± 0.11	+0.80	1.75	0.53	80.1	1.84	81.9	0.06	0.30
		B-23-8	15		+0.67 ± 0.02	+0.70	1.33	0.42	84.3	1.77	86.0	0.06	0.32
		B-23-7	11		+0.86 ± 0.06	+0.89	0.92	0.22	86.1	1.67	87.8	0.05	0.24

The corrected $\delta^{98/95}$Mo values were calculated using the formula $\delta^{98/95}Mo_{auth} = [(\delta^{98/95}Mo_{tot} \times Mo_{tot} - \delta^{98/95}Mo_{det} \times Mo_{det})/Mo_{auth}]$, in which the detrital Mo concentration (Mo_{det}) was $Mo_{det} = [(Mo/Al)_{crust} \times Al_{tot}]$ and the authigenic Mo concentration was $Mo_{auth} = [Mo_{tot} - Mo_{det}]$. We applied a detritus correction assuming a Mo concentration of 1.1 μg/g, an upper crustal Al_2O_3 concentration of 15.4 wt% (all values from Rudnick and Gao, 2003), and a Mo isotopic composition of 0.0‰ as proposed by Voegelin et al. (2009). For the samples from Bed 27 to Bed 32, due to their low Mo concentrations (far less than the upper crustal mean value which is about 1.1 μg/g) and high Al concentrations, the recalculated authigenic Mo concentrations are very low or even negative using the recalculation method of Al mentioned, so we did not recalculate the corrected $\delta^{98/95}$Mo values of these samples. Ca + Mg: $CaCO_3$ (%) + $MgCO_3$ (%). The Al and Mn/Sr data are from Zhang et al. (2018).

values of +1.03‰ and + 1.17‰, respectively. Their authigenic Mo contents are negative when Al is used to recalculate $\delta^{98/95}$Mo values; however, their $\delta^{98/95}$Mo values are higher than those of terrigenous detritus. We conclude that authigenic Mo dominated the $\delta^{98/95}$Mo values of these two samples, and that the $\delta^{98/95}$Mo values of the authigenic Mo should be higher than the acquired values.

From Bed 23 to the middle of Bed 24 in the Meishan section, the $\delta^{98/95}Mo_{corr.Al}$ values gradually decrease from +0.89‰ to +0.35‰, while from the middle of Bed 24 to Bed 25, the $\delta^{98/95}Mo_{corr.Al}$ values gradually increase from +0.35‰ to +1.78‰ (Fig. 4a). Based on these results and the hypothesis discussed above, these Mo isotopic variations indicate that the oceanic paleo-redox conditions gradually became more oxic from Bed 23 to the middle of Bed 24, and then gradually transitioned toward a lack of oxygen from the middle of Bed 24 to Bed 25. The $\delta^{98/95}Mo_{corr.Al}$ values from Bed 23 to the top of Bed 24 (B-23-7 to B-24-8, interval 1 in Fig. 4a) vary from +0.35‰ to +0.89‰ (+0.65‰ on average), which fall within the reported $\delta^{98/95}$Mo range of suboxic sediments (−0.5‰ to +1.3‰; Poulson et al., 2006; Siebert et al., 2006), suggesting a suboxic paleo-ocean environment during this period. The $\delta^{98/95}Mo_{corr.Al}$ values from the uppermost part of Bed 24e (B-24-9) to

Table 5
Molybdenum isotope composition and major elemental contents (Mo, Al, $CaCO_3$, $MgCO_3$, and Mn/Sr) of the Dajiang section samples.

Samples	Position (cm)	Lithology	$\delta^{98/95}$Mo (‰) (2SD, N = 3)	$\delta^{98/95}Mo_{corr.Al}$ (‰)	Mo (μg/g)	Al (%)	$CaCO_3$ (%)	$MgCO_3$ (%)	Ca + Mg (%)	Mn/Sr
TDJ-15	1372	microbialite	−0.02 ± 0.06	−0.03	0.14	0.15	82.3	6.37	88.7	0.68
TDJ-14	1272		−0.20 ± 0.07	−0.25	0.22	0.33	77.5	12.3	89.8	0.92
TDJ-12	1172		+0.12 ± 0.07	+0.14	0.34	0.22	73.5	17.5	91.0	0.76
TDJ-11	822		+0.37 ± 0.08	+0.45	0.25	0.32	60.0	33.6	93.6	0.75
TDJ-10	472		+0.05 ± 0.07	+0.05	0.16	0.09	81.8	9.80	91.6	0.33
TDJ-9	312		+0.09 ± 0.09	+0.09	0.23	0.01	83.3	10.3	93.6	0.32
TDJ-8	192		+0.65 ± 0.06	+0.66	0.26	0.03	90.0	4.17	94.2	0.21
TDJ-7	142		+0.83 ± 0.12	+0.83	2.67	0.15	87.0	3.01	90.0	0.26
TDJ-6	102		−0.08 ± 0.06	−0.08	0.12	0.01	90.8	1.23	92.0	0.27
TDJ-4	52		+0.25 ± 0.11	+0.26	0.13	0.01	89.5	1.16	90.7	0.24
TDJ-3	32		+1.45 ± 0.04	+1.49	0.75	0.16	89.0	1.75	90.8	0.27
TDJ-2	22		+1.42 ± 0.14	+1.55	0.23	0.15	88.5	3.99	92.5	0.16
TDJ-1-3	12		+1.46 ± 0.12	+1.62	0.22	0.16	87.5	12.0	99.5	0.22
TDJ-1-2	8		+1.56 ± 0.09	+1.63	0.21	0.06	81.0	12.9	93.9	0.35
TDJ-1-1	4		+1.32 ± 0.13	+1.38	0.20	0.06	80.5	15.3	95.8	0.35
PDJ-0	−2.5	packstone	+0.27 ± 0.11	+0.28	0.18	0.05	92.3	1.09	93.4	0.17
PDJ-1	−5		+0.45 ± 0.12	+0.46	0.13	0.03	89.3	1.16	90.5	0.20
PDJ-2	−15		+0.22 ± 0.12	+0.23	0.16	0.04	91.3	1.05	92.4	0.19
PDJ-3	−25		+0.30 ± 0.03	+0.31	0.15	0.04	91.0	1.19	92.2	0.22
PDJ-4	−35		+0.15 ± 0.12	+0.15	0.16	0.02	89.5	0.91	90.4	0.25
PDJ-5	−80		+0.40 ± 0.08	+0.40	0.27	0.02	91.8	1.65	93.5	0.29
PDJ-7	−180		−0.05 ± 0.03	−0.05	0.21	0.01	90.0	1.05	91.1	0.36
PDJ-8	−230		−0.04 ± 0.05	−0.04	0.12	0.01	86.5	4.59	91.1	0.48
PDJ-10	−550		−0.01 ± 0.02	−0.01	0.13	0.02	87.0	2.63	89.6	0.32

Ca + Mg: $CaCO_3$ (%) + $MgCO_3$ (%).

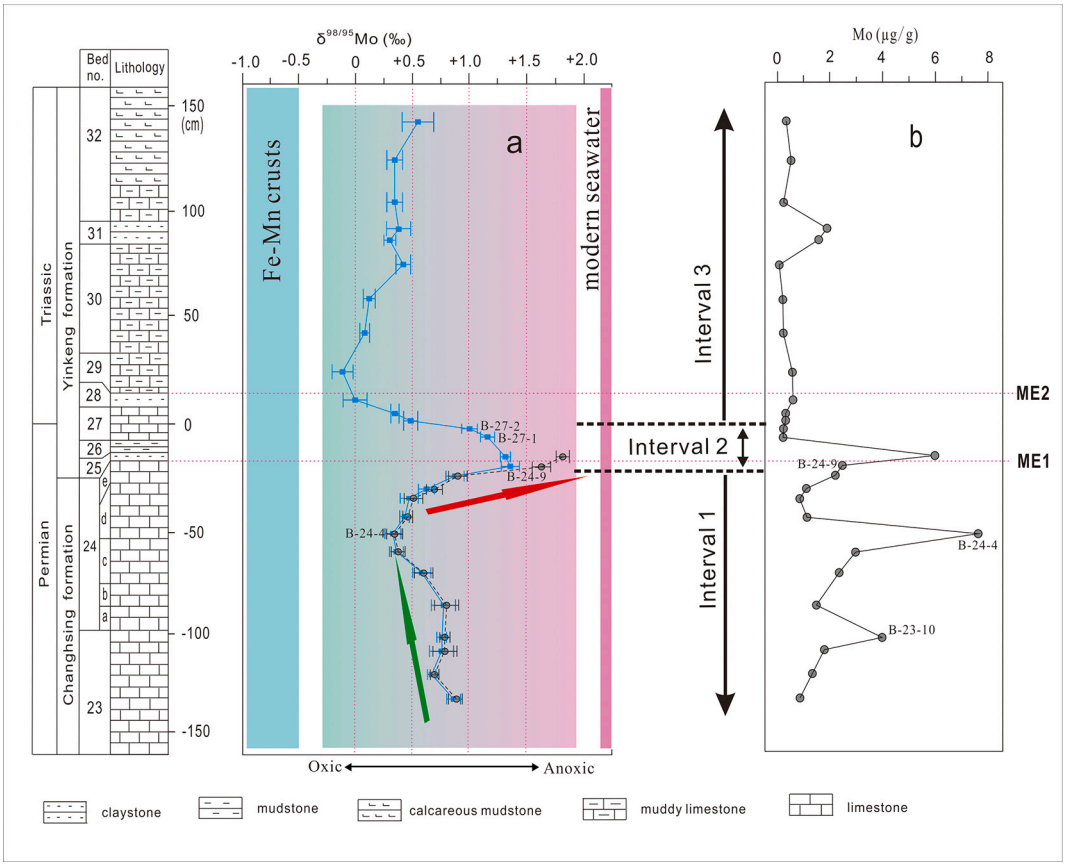

Fig. 4. Stratigraphic record of $\delta^{98/95}$Mo values and Mo contents in the Meishan section. (a) Measured $\delta^{98/95}$Mo values (blue squares) and Al-corrected $\delta^{98/95}$Mo values (grey circles). The lines marked ME1 and ME2 indicate the starting horizons of the two episodes of mass extinction events (Song et al., 2013). (For interpretation of the references to colour in this figure legend, the reader is referred to the web version of this article.)

Bed 25 vary from +1.56‰ to +1.78‰ (+1.67‰ on average), which is consistent with the $\delta^{98/95}$Mo values of open-ocean anoxic sediments (approximately +1.6‰) reported by Poulson et al. (2006). Furthermore, the $\delta^{98/95}Mo_{corr.Al}$ value (+1.78‰) of Bed 25 is consistent with the maximum $\delta^{98/95}$Mo value (+1.76‰) of the upper Permian Thuringian Basin sediments (Ruebsam et al., 2017), which formed in a semi-

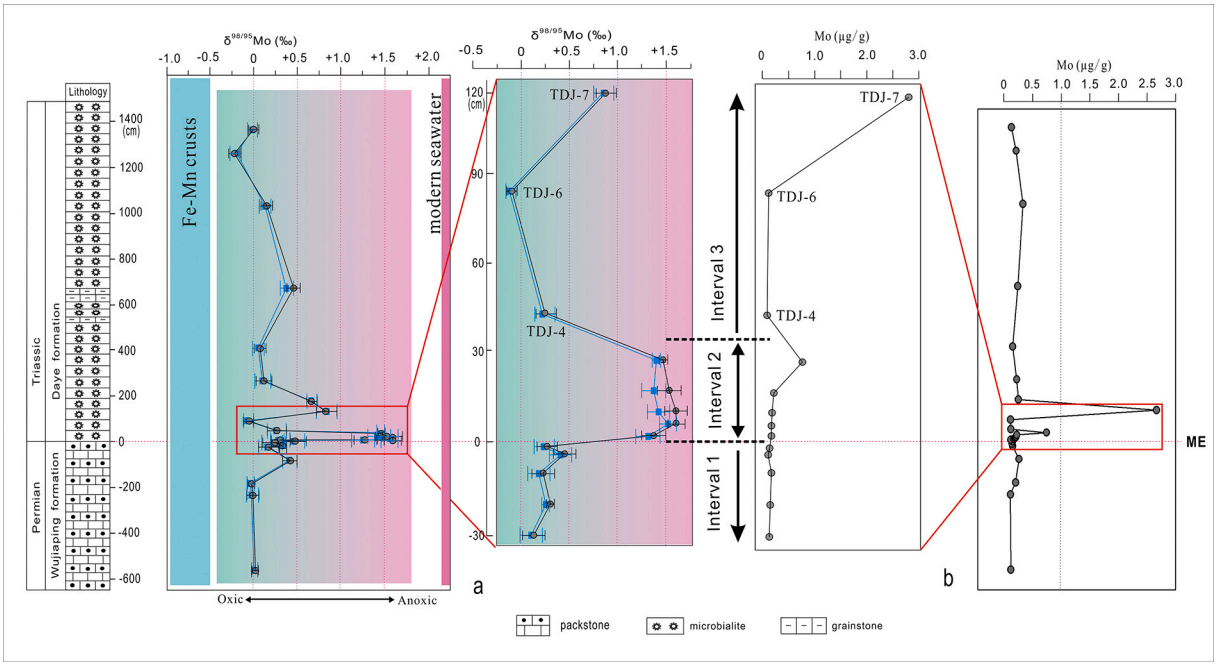

Fig. 5. Stratigraphic record of $\delta^{98/95}$Mo values and Mo contents in the Dajiang section. (a) Measured $\delta^{98/95}$Mo values (blue squares) and Al-corrected $\delta^{98/95}$Mo values (grey circles). The lines marked ME indicate the starting horizons of the mass extinction events (Ezaki et al., 2003; Jiang et al., 2014; Song et al., 2014). (For interpretation of the references to colour in this figure legend, the reader is referred to the web version of this article.)

enclosed intracontinental basin with a narrow connection to the global ocean (Wuchiapingian; ca. 256 Ma) (e.g., Vaughan et al., 1989; Grice et al., 1997; Ruebsam et al., 2017) and are characterized by typical anoxic deposition in an open marine environment (Ruebsam et al., 2017). Therefore, we suggest that the paleo-ocean was anoxic during the deposition of the uppermost part of Bed 24e to Bed 25 in the Meishan section. This variation in redox conditions, reflected by Mo isotopes, is consistent with the results of studies of pyrite framboids from the same section (Shen et al., 2007; Chen et al., 2015).

5.2.3. *$\delta^{98/95}$Mo and oceanic paleo-redox conditions of the Dajiang section*

The variation in the $\delta^{98/95}Mo_{corr.Al}$ values of the Dajiang section are reported in Fig. 5a. The samples below the mass extinction boundary have lower $\delta^{98/95}Mo_{corr.Al}$ values and little variability (from −0.05‰ to +0.46‰, +0.19‰ on average; interval 1 in Fig. 5a), while the $\delta^{98/95}Mo_{corr.Al}$ values of five samples above and near the mass extinction boundary increase abruptly (from +1.38‰ to +1.63‰; +1.53‰ on average; interval 2 in Fig. 5a). This trend indicates that ocean anoxia occurred suddenly, which is consistent with the onset of the mass extinction event.

In general, the variation in $\delta^{98/95}$Mo values in the Dajiang section (Fig. 5a) is consistent with that in the Meishan section (Fig. 4a). That is, before the mass extinction event, the $\delta^{98/95}$Mo values of both sections were relatively lower (interval 1 in Figs. 4a and 5a), and the values were higher during the relatively short interval coinciding with the mass extinction (interval 2 in Figs. 4a and 5a). The values of both sections decreased after the mass extinction event and returned to pre-extinction values (interval 3 in Figs. 4a and 5a).

5.3. *Changing ocean redox conditions during the Permian–Triassic transition*

In the two sections studies here, the $\delta^{98/95}$Mo values of the bulk carbonate samples covary with the oxidized and sulfided Mo contents. In the portion of the section where the $\delta^{98/95}$Mo values increase gradually, the contents of oxidized Mo decrease gradually and the contents of sulfided Mo increase gradually. In contrast, when the values of $\delta^{98/95}$Mo decrease gradually, the contents of oxidized Mo increase gradually and the contents of sulfided Mo decrease gradually. This covariance might indicate that the Mo isotopic signal of bulk carbonate samples records the overall redox state of the ocean.

For the Dajiang section, which was deposited on a shallow platform, $\delta^{98/95}$Mo values indicate that oceanic anoxia was nearly coincident with the mass extinction event. For the Meishan section, which was deposited on a relatively deep-water platform-margin slope, Song et al. (2013) divided the mass extinction event into two episodes: the first episode (main episode) began at the bottom of Bed 25 and the second episode began at the top of Bed 28. According to this division, the $\delta^{98/95}$Mo values indicate that ocean anoxia slightly preceded the mass extinction event in the Meishan section.

The $\delta^{98/95}$Mo values of both sections decreased after the mass extinction event and returned to pre-extinction values (interval 3 in Figs. 4a and 5a). In the Meishan section, the high Al/Mo ratios of some samples mean we cannot determine if the Mo has a terrigenous detrital or authigenic origin, whereas for the Dajiang section the Mo is primarily authigenic Mo. Local and global marine redox conditions effect the $\delta^{98/95}$Mo value of sediments (Barling and Anbar, 2004; Anbar and Rouxel, 2007; Kendall et al., 2017). Prior to anoxic events, the paleo-ocean would have been oxidized, and if anoxia was global in scale the proportion of ancient seawater Mo removed to anoxic versus oxic sinks would have changed dramatically as the oxic sink fluxes of ancient seawater Mo (mainly Mo in seawater adsorbed by Fe-Mn oxides) decreased and the anoxic sink fluxes of seawater Mo increased (Barling and Anbar, 2004; Anbar and Rouxel, 2007; Kendall et al., 2017; Chen et al., 2019). This would have led to a gradual decrease in the $\delta^{98/95}$Mo values of ancient seawater (Chen et al., 2019). Therefore, there may be two reasons why the $\delta^{98/95}$Mo values of the Dajiang section returned to pre-extinction values after the mass extinction event (interval 3 in Fig. 5a): 1) the ocean gradually returned to its original oxidation state after a relatively short period of anoxia; or 2) long-term ocean anoxia led to a gradual decrease in the amount of Mo adsorbed by Fe-Mn oxides, eventually leading to a decrease in the $\delta^{98/95}$Mo value of seawater. The estimated $\delta^{98/95}$Mo values of ancient seawater do not show a decreasing trend during the anoxic event in either section (Fig. 2), and in the Dajiang

section, as the $\delta^{98/95}$Mo values of bulk carbonate samples return to the pre-extinction level, the $\delta^{98/95}$Mo values of corresponding ancient seawater are also roughly the same as those before the extinction (Fig. 2b). Previous studies have shown that some sections do not record anoxia during the end-Permian extinction event (Proemse et al., 2013; Xiang et al., 2016); and based on the model, ~18% of the paleo-ocean was anoxic during the main episode of the extinction event, with anoxia mainly occurring in continental shelf areas (Zhang et al., 2020). We therefore infer that although a large proportion of ancient seawater was anoxic at the PTB, the whole ocean was still only "partially" anoxic, and therefore ocean anoxia may have had little effect on the $\delta^{98/95}$Mo value of ancient seawater. Hence, a decrease in the $\delta^{98/95}$Mo values of carbonate samples after the extinction event may imply a gradual return of the ocean to its earlier oxidation state.

In the Dajiang section, the total thickness of the five samples whose $\delta^{98/95}$Mo values increase abruptly is 32 cm, which implies that oceanic anoxia lasted for a short time. The layer at ~15 m above the extinction boundary falls within the *H. parvus* zone (Jiang et al., 2014). High-precision zircon U-Pb dating of the Meishan section demonstrates that this zone lasted for <0.061 Myr (Burgess et al., 2014), indicating that the oceanic anoxia lasted for <0.061 Myr.

6. Conclusions

1. The Mo isotopic signature of carbonates deposited in open-ocean settings reflects the three types of Mo precipitation that occur in ancient seawater; i.e., Mo preserved in carbonate sediments in the form of pore water or inclusions, absorbed oxidized Mo, and sulfided Mo. These data reveal the dominant accumulation mechanism of authigenic Mo. We suggest that marine carbonate sediments can record the paleo-ocean Mo isotopic signal, and the mechanism is similar to that of other open-ocean sediments (e.g., shales), with higher $\delta^{98/95}$Mo values representing a more reducing sedimentary environment.
2. Variations in the $\delta^{98/95}$Mo values of the Meishan and Dajiang sections indicate that during the Permian–Triassic transition, oceanic anoxia coincided with or slightly predated the mass extinction event and lasted for a short time, likely <0.061 Myr.

Declaration of Competing Interest

The authors declare that they have no known competing financial interests or personal relationships that could have appeared to influence the work reported in this paper.

Acknowledgments

This work was financially supported by the Strategic Priority Research Program (B) of Chinese Academy of Sciences (XDB18000000) and the National Natural Science Foundation of China (Nos. 41573007 and 41173026). We thank Professor Yanan Shen and an anonymous reviewer for their constructive comments on the initial version of this manuscript. We also thank editor Michael E. Böttcher for comments that improved the manuscript.

Appendix A. Supplementary data

Supplementary data to this article can be found online at https://doi.org/10.1016/j.chemgeo.2021.120259.

References

Algeo, T.J., Tribovillard, N., 2009. Environmental analysis of paleoceanographic systems based on molybdenum-uranium covariation. Chem. Geol. 268, 211–225.
Algeo, T.J., Hannigan, R., Rowe, H., Brookfield, M., Baud, A., Krystyn, L., Ellwood, B.B., 2007. Sequencing events across the Permian–Triassic boundary, Guryul Ravine (Kashmir,India). Palaeogeogr. Palaeoclimatol. Palaeoecol. 252, 328–346.
Algeo, T.J., Kuwahara, K., Sano, H., Bates, S., Lyons, T., Elswick, E., Hinnov, L., Ellwood, B., Moser, J., Maynard, J.B., 2011. Spatial variation in sediment fluxes, redox conditions,and productivity in the Permian-Triassic Panthalassic Ocean. Palaeogeogr. Palaeoclimatol. Palaeoecol. 308, 65–83.
Anbar, A.D., 2004. Molybdenum stable isotopes: observations, interpretations and directions. Mineral. Soc. Am. 55, 429–454.
Anbar, A.D., Rouxel, O., 2007. Metal Stable Isotopes in Paleoceanography. Annu. Rev. Earth Planet. Sci. 35, 717–746. https://doi.org/10.1146/annurev.earth.34.031405.125029.
Arnold, G.L., Anbar, A.D., Barling, J., Lyons, T.W., 2004. Molybdenum isotope evidence for widespread anoxia in Mid-Proterozoic Oceans. Science 304, 87–90.
Barling, J., Anbar, A.D., 2004. Molybdenum isotope fractionation during adsorption by manganese oxides. Earth Planet. Sci. Lett. 217, 315–329.
Barling, J., Arnold, G.L., Anbar, A.D., 2001. Natural mass-dependent variations in the isotopic composition of molybdenum. Earth Planet. Sci. Lett. 193, 447–457.
Bond, D.P.G., Wignall, P.B., 2010. Pyrite framboid study of marine Permian–Triassic boundary sections: a complex anoxic event and its relationship to contemporaneous mass extinction. Geol. Soc. Am. Bull. 122 (7–8), 1265–1279.
Brennecka, G.A., Herrmann, A.D., Algeo, T.J., Anbar, A.D., 2011. Rapid expansion of oceanic anoxia immediately before the end-Permian mass extinction. PNAS 108 (43), 17631–17634.
Bura-Nakić, E., Sondi, J., Mikac, N., Andersen, M.B., 2020. Investigating the molybdenum and uranium redox proxies in a modern shallow anoxic carbonate rich marine sediment setting of the Malo Jezero (Mljet Lakes, Adriatic Sea). Chem. Geol. 533 https://doi.org/10.1016/j.chemgeo.2019.119441.
Burgess, S.D., Bowring, S., Shen, S.Z., 2014. High-precision timeline for Earth's most severe extinction. PNAS 111 (9), 3316–3321.
Cao, C.Q., Zheng, Q.F., 2009. Geological event sequences of the Permian-Triassic transition recorded in the microfacies in Meishan. Sci. China Earth Sci. 52 (10), 1529–1536.
Cao, C., Liu, X.M., Batailleb, C.P., Liu, C., 2020. What do Ce anomalies in marine carbonates really mean? A perspective from leaching experiments. Chem. Geol. 532 https://doi.org/10.1016/j.chemgeo.2019.119413.
Chen, J., Beatty, T.W., Henderson, C.M., Rowe, H., 2009. Conodont biostratigraphy across the Permian–Triassic boundary at the Dawen section, Great Bank of Guizhou, Guizhou Province, South China: Implications for the late Permian extinction and correlation with Meishan. J. Asian Earth Sci. 36, 442–458.
Chen, Z.Q., Yang, H., Luo, M., Benton, M.J., Kaiho, K., Zhao, L.S., Huang, Y.G., Zhang, K.X., Fang, Y.H., Jiang, H.S., Qiu, H., Li, Y., Tu, C.Y., Shi, L., Zhang, L., Feng, X.Q., Chen, L., 2015. Complete biotic and sedimentary records of the Permian–Triassic transition from Meishan section, South China: Ecologically assessing mass extinction and its aftermath. Earth Sci. Rev. 149, 67–107.
Chen, J.B., Zhao, L.S., Algeo, T.J., Zhou, L., Zhang, L., Qiu, H.A., 2019. Evaluation of paleomarine redox conditions using Mo-isotope data in low-[Mo] sediments: a case study from the lower Triassic of South China. Palaeogeogr. Palaeoclimatol. Palaeoecol. 519, 178–193.
Cheng, M., Li, C., Chen, X., Zhou, L., Algeo, T.J., Ling, H.F., Feng, L.J., Jin, C.S., 2018. Delayed Neoproterozoic oceanic oxygenation: evidence from Mo isotopes of the Cryogenian Datangpo Formation. Precambrian Res. 319, 187–197.
Duan, Y., Anbar, A.D., Arnold, G.L., Lyons, T.W., Gordon, G.W., Kendall, B., 2010. Molybdenum isotope evidence for mild environmental oxygenation before the Great Oxidation Event. Geochim. Cosmochim. Acta 74, 6655–6668.
Emerson, S.R., Huested, S.S., 1991. Ocean anoxia and the concentrations of molybdenum and vanadium in seawate. Mar. Chem. 34, 177–196.
Erickson, B.E., Helz, G.R., 2000. Molybdenum(VI) speciation in sulfidic waters: Stability and lability of thiomolybdates. Geochim. Cosmochim. Acta 64, 1149–1158.
Erwin, D.H., 1994. The Permo-Triassic extinction. Nature. 367, 231–236.
Ezaki, Y., Liu, J.B., Adachi, N., 2003. Earliest Triassic microbialite micro- to megastructures in the Huaying area of Sichuan Province, South China: Implications for the nature of oceanic conditions after the end-Permian extinction. Palaios 18 (4/5), 388–402.
Goldberg, T., Archer, C., Vance, D., Poulton, S.W., 2009. Mo isotope fractionation during adsorption to Fe (oxyhydr)oxides. Geochim. Cosmochim. Acta 73, 6502–6516.
Goldberg, T., Gordon, G.W., Izon, G., Archer, C., Pearce, C.R., McManus, J., Anbar, A.D., Rehkämper, M., 2013. Resolution of inter-laboratory discrepancies in Mo isotope data: an intercalibration. J. Anal. At. Spectrom. 28, 724–735.
Greber, N.D., Siebert, C., Nägler, T.F., Pettke, T., 2012. $\triangle^{98/95}$Mo values and molybdenum concentration data for NIST SRM 610, 612 and 3134: towards a common protocol for reporting Mo data. Geostand. Geoanal. Res. 36, 291–300.
Grice, K., Schaeffer, P., Schwark, L., Maxwell, J.R., 1997. Changes in palaeoenvironmental conditions during deposition of the Permian Kupferschiefer (Lower Rhine Basin,northwest Germany) inferred from molecular and isotopic compositions of biomarker components. Org. Geochem. 26, 677–690.
Grice, K., Cao, C.Q., Love, G.D., Bottcher, M.E., Twitchett, R.J., Grosjean, E., Summons, R.E., Turgeon, S.C., Dunning, W., Jin, Y.G., 2005. Photic zone euxinia during the Permian-Triassic superanoxic event. Science 307, 706–709.
He, W.H., Feng, Q.L., Gu, S.Z., Jin, Y.X., 2005. Changxingian (Upper Permian) radiolarian fauna from Meishan D section, Changxing, Zhejiang, China, and its possible paleoecological significance. J. Paleontol. 79 (2), 209–218.
Helz, G.R., Miller, C.V., Charnock, J.M., Mosselmans, J.F.W., Pattrick, R.A.D., Garner, C.D., Vaughan, D.L., 1996. Mechanism of molybdenum removal from the sea and its concentration in black shales: EXAFS evidence. Geochim. Cosmochim. Acta 60 (19), 3631–3642.
Herrmann, A.D., Kendall, B., Algeo, T.J., Gordon, G.W., Wasylenki, L.E., Anbar, A.D., 2012. Anomalous molybdenum isotope trends in Upper Pennsylvanian euxinic

facies: significance for use of δ^{98}Mo as a global marine redox proxy. Chem. Geol. 324-325, 87–98.
Huang, S.J., Qing, H.R., Huang, P.P., Hu, Z.W., Wang, Q.D., Zou, M.L., Liu, H.N., 2008. Evolution of strontium isotopic composition of seawater from late Permian to early Triassic based on study of marine carbonates, Zhongliang Mountain, Chongqing, China. Sci. China Earth Sci. 51 (4), 528–539.
Isozaki, Y., 1997. Permo-Triassic boundary superanoxia and stratified superocean: Records from lost deep sea. Science 276, 235–238.
Jiang, H.S., Lai, X.L., Sun, Y.D., Wignall, P.B., Liu, J.B., Yan, C.B., 2014. Permian–Triassic Conodonts from Dajiang (Guizhou, South China) and their implication for the age of microbialite deposition in the Aftermath of the end-Permian mass extinction. J. Earth Sci. 25 (3), 413–430.
Jin, Y.G., Wang, Y., Wang, W., Shang, Q.H., Cao, C.Q., Erwin, D.H., 2000. Pattern of marine mass extinction near the Permian-Triassic boundary in South China. Science. 289, 432–436.
Kakuwa, Y., Matsumoto, R., 2006. Cerium negative anomaly just before the Permian and Triassic boundary event—the upward expansion of anoxia in the water column. Palaeogeogr. Palaeoclimatol. Palaeoecol. 229, 335–344.
Kendall, B., Creaser, R.A., Gordon, G.W., Anbar, A.D., 2009. Re-Os and Mo isotope systematics of black shales from the Middle Proterozoic Velkerri and Wollogorang Formations, McArthur Basin, northern Australia. Geochim. Cosmochim. Acta 73 (9), 2534–2558.
Kendall, B., Gordon, G.W., Poulton, S.W., Anbar, A.D., 2011. Molybdenum isotope constraints on the extent of late Paleoproterozoic Ocean euxinia. Earth Planet. Sci. Lett. 307, 450–460.
Kendall, B., Dahl, T.W., Anbar, A.D., 2017. The stable isotope geochemistry of molybdenum. Rev. Mineral. Geochem. 82, 683–732.
Kurzweil, F., Wille, M., Gantert, N., Beukes, N.J., Schoenberg, R., 2016. Manganese oxide shuttling in pre-GOE oceans - evidence from molybdenum and iron isotopes. Earth Planet. Sci. Lett. 452, 69–78.
Lau, K.V., Maher, K., Altiner, D., Kelley, B.M., Kump, L.R., Lehrmann, D.J., Silva-Tamayo, J.C., Weaver, K.L., Yu, M.Y., Payne, J.L., 2016. Marine anoxia and delayed Earth system recovery after the end-Permian extinction. PNAS. https://doi.org/10.1073/pnas.1515080113.
Lehrmann, D.J., Wei, J.Y., Enos, P., 1998. Controls on facies architecture of a large Triassic carbonate platform; the Great Bank of Guizhou, Nanpanjiang Basin, South China. J. Sediment. Res. 68 (2), 311–326.
Lehrmann, D.J., Payne, J.L., Felix, S.V., Dillett, P.M., Wang, H.M., Yu, Y.Y., Wei, J.Y., 2003. Permian-triassic boundary sections from shallow-marine carbonate platforms of the Nanpanjiang Basin, South China: implications for Oceanic conditions associated with the end-permian extinction and its Aftermath. PALAIOS 18, 138–152.
Lehrmann, D.J., Enos, P., Payne, J.L., Montgomery, P., Wei, J.Y., Yu, Y.Y., Xiao, J.F., Orchard, M.J., 2005. Permian and Triassic depositional history of the Yangtze platform and Great Bank of Guizhou in the Nanpanjiang Basin of Guizhou and Guangxi, South China. Albertiana 33, 149–168.
Li, J., Zhu, X.K., Tang, S.H., 2011. The application of double spike in non-traditional stable isotope—a case study of Mo isotopes. Rock Miner. Anal. 30 (2), 138–143 (in Chinese with English abstract).
Li, G.S., Wang, Y.B., Shi, G.R., Liao, W., Yu, L.X., 2015a. Fluctuations of redox conditions across the Permian-Triassic boundary-New evidence from the GSSP section in Meishan of South China. Palaeogeogr. Palaeoclimatol. Palaeoecol. https://doi.org/10.1016/j.palaeo.2015.09.050.
Li, J., Zhu, X.K., Tang, S.H., Zhang, K., 2015b. High-precision measurement of molybdenum isotopic compositions of selected geochemical reference materials. Geostand. Geoanal. Res. 40, 405–415.
Liu, J., Wen, H.J., Zhang, Y.X., Fan, H.F., Zhu, C.W., 2016. Precise Mo isotope ratio measurements of low-Mo (ng g-1) geological samples using MC-ICP-MS. J. Anal. At. Spectrom. 31, 1287–1297.
Magnall, J.M., Gleeson, S.A., Poulton, S.W., Gordon, G.W., Paradis, S., 2018. Links between seawater paleoredox and the formation of sediment-hosted massive sulphide (SHMS) deposits — Fe speciation and Mo isotope constraints from late Devonian mudstones. Chem. Geol. 490, 45–60.
Nägler, T.F., Siebert, C., Lüschen, H., Böttcher, M.E., 2005. Sedimentary Mo isotope record across the Holocene fresh-brackish water transition of the Black Sea. Chem. Geol. 219, 283–295.
Nägler, T.F., Anbar, A.D., Archer, C., Goldberg, T., Gordon, G.W., Greber, N.D., Siebert, C., Sohrin, Y., Vance, D., 2014. Proposal for an international molybdenum isotope measurement standard and data representation. Geostand. Geoanal. Res. 38, 149–151.
Neubert, N., Nägler, T.F., Bottcher, M.E., 2008. Sulfidity controls molybdenum isotope fractionation into euxinic sediments: evidence from the modern Black Sea. Geology 36 (10), 775–778.
Nie, S., 1991. Paleoclimatic and paleomagnetic constraints on the Paleozoic reconstructions of South China, North China and Tarim. Tectonophysics 196, 279–308.
Nothdurft, L.D., Webb, G.E., Kamber, B.S., 2004. Rare earth element geochemistry of late Devonian reefal carbonates, Canning Basin, Western Australia: Confirmation of a seawater REE proxy in ancient limestones. Geochim. Cosmochim. Acta 68, 263–283.
Poulson, R.L., Siebert, C., McManus, J., Berelson, W.M., 2006. Authigenic molybdenum isotope signatures in marine sediments. Geology 34, 617–620.
Poulson-Brucker, R.L., McManus, J., 2009. Molybdenum behavior during early diagenesis: Insights from Mo isotopes. Geochem. Geophys. Geosyst. 10 (2008GC002180).
Proemse, B.C., Grasby, S.E., Wieser, M.E., Mayer, B., Beauchamp, B., 2013. Molybdenum isotopic evidence for oxic marine conditions during the latest Permian extinction. Geology 41, 967–970.
Rock and mineral analysis group, 2011. Rock and Mineral Analysis, , Fourth ed.3. Geology Publishing House, Beijing, pp. 357–359. in China.
Rongemaille, E., Bayon, G., Pierre, C., Bollinger, C., Chu, N.C., Fouquet, Y., Riboulot, V., Voisset, M., 2011. Rare earth elements in cold seep carbonates from the Niger delta. Chem. Geol. 286, 196–206.
Rudnick, R.L., Gao, S., 2003. Composition of the continental crust. In: Rudnick, R.L. (Ed.), The Crust, Vol. 3 of Treatise on Geochemistry (Holland H D, Turekian K K eds.), pp. 1–64.
Ruebsam, W., Dickson, A.J., Hoyer, E.M., Schwark, L., 2017. Multiproxy reconstruction of oceanographic conditions in the southern epeiric Kupferschiefer Sea (late Permian) based on redox-sensitive trace elements, molybdenum isotopes and biomarkers. Gondwana Res. 44, 205–218.
Scheiderich, K., Zerkle, A.L., Helz, G.R., Farquhar, J., Walker, R.J., 2010. Molybdenum isotope, multiple sulfur isotope, and redox-sensitive element behavior in early Pleistocene Mediterranean sapropels. Chem. Geol. 279, 134–144.
Scott, C., Lyons, T.W., 2012. Contrasting molybdenum cycling and isotopic properties in euxinic versus non-euxinic sediments and sedimentary rocks: refining the paleoproxies. Chem. Geol. 324-325, 19–27.
Shen, W.J., Lin, Y.T., Xu, L., Li, J.F., Wu, Y.S., Sun, Y.G., 2007. Pyrite framboids in the Permian–Triassic boundary section at Meishan, China: evidence for dysoxic deposition. Palaeogeogr. Palaeoclimatol. Palaeoecol. 253, 323–331.
Shen, Y.A., Farquhar, J., Zhang, H., Masterson, A., Zhang, T.G., Wing, B.A., 2011. Multiple S-isotopic evidence for episodic shoaling of anoxic water during late Permian mass extinction. Nat. Commun. 2 (1), 116–119.
Siebert, C., Nägler, T.F., Kramers, J.D., 2001. Determination of molybdenum isotope fractionation by doublespike multicollector inductively coupled plasma mass spectrometry. Geochem. Geophys. Geosyst. 2 (2000GC000124).
Siebert, C., Nägler, T.F., von Blanckenburg, F., Kramers, J.D., 2003. Molybdenum isotope records as a potential new proxy for paleoceanography. Earth Planet. Sci. Lett. 211, 159–171.
Siebert, C., McManus, J., Bice, A., Poulson, R., Berelson, W.M., 2006. Molybdenum isotope signatures in continental margin marine sediments. Earth Planet. Sci. Lett. 241, 723–733.
Song, H.J., Wignall, P.B., Tong, J.N., Yin, H.F., 2013. Two pulses of extinction during the Permian–Triassic crisis. Nat. Geosci. 6, 52–56.
Song, H.Y., Tong, J.N., Tian, L., Song, H.J., Qiu, H.O., Zhu, Y.Y., Algeo, T., 2014. Paleo-redox conditions across the Permian-Triassic boundary in shallow carbonate platform of the Nanpanjiang Basin, South China. Sci. China Earth Sci. 57, 1030–1038. https://doi.org/10.1007/s11430-014-4843-2.
Tossell, J.A., 2005. Calculating the partitioning of the isotopes of Mo between oxidic and sulfidic species in aqueous solution. Geochim. Cosmochim. Acta 69, 2981–2993.
Vaughan, D.J., Sweeney, M., Friedrich, G., Diedel, R., Haranczyk, C., 1989. The Kupferschiefer: an overview with an appraisal of the different types of mineralization. Econ. Geol. 84, 1003–1027.
Voegelin, A.R., Nägler, T.F., Samankassou, E., Villa, I.M., 2009. Molybdenum isotopic composition of modern and carboniferous carbonates. Chem. Geol. 265, 488–498.
Voegelin, A.R., Nägler, T.F., Beukes, N.J., Lacassie, J.P., 2010. Molybdenum isotopes in late Archean carbonate rocks: Implications for early Earth oxygenation. Precambrian Res. 182, 70–82.
Wasylenki, L.E., Rolfe, B.A., Weeks, C.L., Spiro, T.G., Anbar, A.D., 2008. Experimental investigation of the effects of temperatureand ionic strength on Mo isotope fractionation during adsorption to manganese oxides. Geochim. Cosmochim. Acta 72, 5997–6005.
Wen, H.J., Carignan, J., Cloquet, C., Zhu, X.K., Zhang, Y.X., 2010. Isotopic delta values of molybdenum standard reference and prepared solutions measured by MC-ICP-MS: proposition for delta zero and secondary references. J. Anal. At. Spectrom. 25, 716–721.
Wen, H.J., Carignan, J., Zhang, Y.X., Fan, H.F., Cloquet, C., Liu, S.R., 2011. Molybdenum isotopic records across the Ediacaran Cambrian boundary. Geology 39, 775–778.
Wen, H.J., Fan, H.F., Zhang, Y.X., Cloquet, C., Carignan, J., 2015. Reconstruction of early Cambrian Ocean chemistry from Mo isotopes. Geochim. Cosmochim. Acta 164, 1–16.
Wignall, P.B., Newton, R., 1998. Pyrite framboid diameter as a measure of oxygen deficiency in ancient mudrocks. Am. J. Sci. 298, 537–552.
Wignall, P.B., Twitchett, R.J., 1996. Oceanic anoxia and the end Permiannmass extinction. Science 272, 1155–1158.
Wignall, P.B., Twitchett, R.J., 2002. Extent, duration, and nature of the Permian-Triassic superanoxic event. Geol. Soc. Am. 356, 395–413. https://doi.org/10.1130/0-8137-2356-6.395.
Wignall, P.B., Newton, R., Brookfield, M.E., 2005. Pyrite framboid evidence for oxygen-poor deposition during the Permian-Triassic crisis in Kashmir. Palaeogeogr. Palaeoclimatol. Palaeoecol. 216, 183–188.
Wille, M., Kramers, J.D., Nägler, T.F., Beukes, N.J., Schröder, S., Meisel, T., Lacassie, J.P., Voegelin, A.R., 2007. Evidence for a gradual rise of oxygen between 2.6 and 2.5 Ga from Mo isotopes and Re-PGE signatures in shales. Geochim. Cosmochim. Acta 71, 2417–2435.
Xiang, L., Schoepfer, S.D., Zhang, H., Yuan, D.X., Cao, C.Q., Zheng, Q.F., Henderson, C. M., Shen, S.Z., 2016. Oceanic redox evolution across the end-Permian mass extinction at Shangsi, South China. Palaeogeogr. Palaeoclimatol. Palaeoecol. 448, 59–71.
Xie, S.C., Pancost, R.D., Yin, H.F., Wang, H.M., Evershed, R.P., 2005. Two episodes of microbial change coupled with Permo/Triassic faunal mass extinction. Nature 434, 494–497.

Yang, Z.Y., Wu, S.B., Yin, H.F., Xu, G.R., Zhang, K.X., Bi, X.M., 1993. Permo-Triassic Events of South China. Geological Publishing House, Beijing.
Yin, H.F., 1996. The Palaeozoic-Mesozoic Boundary, Candidates of Global Stratotype Section and Point of the Permian-Triassic Boundary. China University of Geosciences Press, Wuhan.
Yin, H.F., Song, H.J., 2013. Mass extinction and Pangea integration during the Paleozoic-Mesozoic transition. Sci. China Earth Sci. 56, 1791–1803. https://doi.org/10.1007/s11430-013-4624-3.
Yin, H.F., Zhang, K.X., Tong, J.N., Yang, Z.Y., Wu, S.B., 2001. The global stratotype section and point (GSSP) of the Permian-Triassic boundary. Episodes 24, 102–114.
Yin, H.F., Feng, Q.L., Lai, X.L., Baud, A., Tong, J.N., 2007. The protracted Permo-Triassic crisis and multi-episode extinction around the Permian–Triassic boundary. Glob. Planet. Chang. 55, 1–20.
Yin, H.F., Jiang, H.S., Xia, W.C., Feng, Q.L., Zhang, N., Shen, J., 2014. The end-Permian regression in South China and its implication on mass extinction. Earth Sci. Rev. 137, 19–33.
Zhang, Y.X., Wen, H.J., Fan, H.F., 2009. Chemical pretreatment methods for measurement of Mo isotope ratio on geological samples. Chin. J. Anal. Chem. 37, 216–220 (in Chinese with English abstract).
Zhang, Y.X., Wen, H.J., Zhu, C.W., Fan, H.F., Cloquet, C., 2018. Cadmium isotopic evidence for the evolution of marine primary productivity and the biological extinction event during the Permian-Triassic crisis from the Meishan section, South China. Chem. Geol. 481, 110–118.
Zhang, F.F., Shen, S.Z., Cui, Y., Lenton, T.M., Dahl, T.W., Zhang, H., Zheng, Q.F., Wang, W.Q., Krainer, K., Anbar, A.D., 2020. Two distinct episodes of marine anoxia during the Permian-Triassic crisis evidenced by uranium isotopes in marine dolostones. Geochim. Cosmochim. Acta. https://doi.org/10.1016/j.gca.2020.01.032.
Zheng, Y., Anderson, R.F., van Geen, A., Kuwabara, J., 2000. Authigenic molybdenum formation in marine sediments: a link to pore water sulfide in the Santa Barbara Basin. Geochim. Cosmochim. Acta 64 (24), 4165–4178.
Zhou, L., Su, J., Huang, J.H., Yan, J.X., Xie, X.N., Gao, S., Dai, M.N., Tonger, 2011. A new paleoenvironmental index for anoxic events-Mo isotopes in black shales from Upper Yangtze marine sediments. Sci. China Earth Sci. 54, 1024–1033. https://doi.org/10.1007/s11430-011-4188-z.
Zhou, L., Wignall, P.B., Su, J., Feng, Q.L., Xie, S.C., Zhao, L.S., Huang, J.H., 2012. U/Mo ratios and $\delta^{98/95}$Mo as local and global redox proxies during mass extinction events. Chem. Geol. 324-325, 99–107.
Ziegler, P.A., 1988. Evolution of the Arctic-North Atlantic and the Western Tethys. AAPG Mem. 43 (198p).